UNSTEADY AERODYNAMIC FORCE SENSING FROM MEASURED STRAIN

Chan-gi Pak
NASA Armstrong Flight Research Center, Edwards, California 93523-0273

Abstract

A simple approach for computing unsteady aerodynamic forces from simulated measured strain data is proposed in this study. First, the deflection and slope of the structure are computed from the unsteady strain using the two-step approach. Velocities and accelerations of the structure are computed using the autoregressive moving average model, on-line parameter estimator, low-pass filter, and a least-squares curve fitting method together with analytical derivatives with respect to time. Finally, aerodynamic forces over the wing are computed using modal aerodynamic influence coefficient matrices, a rational function approximation, and a time-marching algorithm. A cantilevered rectangular wing built and tested at the NASA Langley Research Center (Hampton, Virginia, USA) in 1959 is used to validate the simple approach. Unsteady aerodynamic forces as well as wing deflections, velocities, accelerations, and strains are computed using the CFL3D computational fluid dynamics (CFD) code and an MSC/NASTRAN code (MSC Software Corporation, Newport Beach, California, USA), and these CFL3D-based results are assumed as measured quantities. Based on the measured strains, wing deflections, velocities, accelerations, and aerodynamic forces are computed using the proposed approach. These computed deflections, velocities, accelerations, and unsteady aerodynamic forces are compared with the CFL3D/NASTRAN-based results. In general, computed aerodynamic forces based on the lifting surface theory in subsonic speeds are in good agreement with the target aerodynamic forces generated using CFL3D code with the Euler equation. Excellent aeroelastic responses

are obtained even with unsteady strain data under the signal to noise ratio of -9.8dB. The deflections, velocities, and accelerations at each sensor location are independent of structural and aerodynamic models. Therefore, the distributed strain data together with the current proposed approaches can be used as distributed deflection, velocity, and acceleration sensors. This research demonstrates the feasibility of obtaining induced drag and lift forces through the use of distributed sensor technology with measured strain data. An active induced drag control system thus can be designed using the two computed aerodynamic forces, induced drag and lift, to improve the fuel efficiency of an aircraft. Interpolation elements between structural finite element grids and the CFD grids and centroids are successfully incorporated with the unsteady aeroelastic computation scheme. The most critical technology for the success of the proposed approach is the robust on-line parameter estimator, since the least-squares curve fitting method depends heavily on aeroelastic system frequencies and damping factors.

1 Introduction

Reducing fuel consumption for modern aircraft is a goal of the National Aeronautics and Space Administration (NASA) Aeronautics Research Mission Directorate (ARMD). This goal can be accomplished by reducing airframe weight and aerodynamic drag, however, reductions in both for a civil transport aircraft is a challenge that may require extensive design changes for optimization and/or active controls. In general, the same percentage of weight and drag reductions can have a similar effect on fuel savings of a transport aircraft [1].

Real-time measurement of aerodynamic drag force in flight is an essential element for implementing an active drag control technique. Two major sources of aerodynamic drag on a business jet and a long-haul transport aircraft at cruise speed are viscous drag and induced drag, which are approximately 48% - 53% (one half) and 21% - 38% (one third) of the total aerodynamic drag [1]. Moreover, induced drag comprises more than 90% of the total drag during takeoff for a typical transport aircraft.

Traditionally, lift forces over the wing are measured using a pressure gauge; however, the conventional pressure gauge with its associated piping and cabling can create weight and space limitation challenges, and pressure data are available only at the discrete location of the gauge. A new method to measure lift forces is needed in order to overcome the weight and bulk associated with conventional pressure gauges. Development of lightweight distributed sensors is a critical technology which can allow continuous monitoring of aerodynamic surface shape, dynamic loading, and active controls of flexible motion and drag.

Flexible and lightweight optical fibers not only revolutionized telecommunications, but also altered the sensing world. Optical fibers can be used as fiber optic sensors to measure strain and temperature [2]. Fiber optic sensors have been developed to measure co-located strain simultaneously with very high accuracy using fiber Bragg gratings (FBGs) [2]. Specifically, the fiber optic strain sensor (FOSS) uses a series of FBGs to obtain measurements at intervals as small as every millimeter [3] along a fiber and at frequencies of several kHz [4]. The ability of FBGs to operate at such high frequencies makes them an ideal choice for both static and dynamic aerospace applications. The methodology of optically measuring aerodynamic forces described by Lie et al. [5] is developed based on beam deformation theory. A two-camera videogrammetric system is used for optical deformation measurements. The data reduction models for extracting the normal force and pitching moment utilize either the local displacement and slope change or the global beam deformation profile.

The availability of wing deflections, velocities, and accelerations at all element grid points across the structural finite element (FE) model [6, 7] will allow engineers to undertake more accurate, real-time analyses of both internal elastic and inertial forces as well as external aerodynamic forces at any point on the structure. These force values over the entire surface of a structure may also find application in structural health monitoring, active flexible motion control, and active drag reduction.

This paper focuses on a computation of unsteady aerodynamic force over an entire three-dimensional structure based on measured strain information. First, structural deformations of the entire three-dimensional structure are obtained using the two-step approach introduced by Pak [6]. Next, velocities and accelerations are computed using an AutoRegressive Moving Average (ARMA) model, on-line parameter estimator [8], low-pass filter, and a least-squares curve fitting method [9] together with analytical derivatives with respect to time. The unsteady aerodynamic forces are computed from structural deflections, velocities, and accelerations along with linear lifting-surface-based modal aerodynamic influence coefficient (AIC) matrices and a rational function approximation (RFA).

2 Mathematical Background

In this study, external unsteady aerodynamic forces are computed from measured strain data. Simulated strain data using CFL3D [10] / MSC/NASTRAN *(MSC Software Corporation, Newport Beach, California, USA)* [11] code will be assumed as measured strain data. In the first section, deflections and slopes of an entire structure are computed from measured strain through the use of the two-step approach [6]. Velocities and accelerations of the structure are computed in the second section using analytical derivatives with respect to time. In the last section, unsteady aerodynamic forces are computed in time-domain using the time-marching algorithm [12].

2.1 Computation of Wing Deflection from Measured Strain

Consider the following structural dynamic governing equations of motion as shown in Eq. (1):

$$[M]\{\ddot{q}\}_k + [G]\{\dot{q}\}_k + [K]\{q\}_k = \{Q_a\}_k \qquad (1)$$

where $[M], [G],$ and $[K]$ are mass, damping, and stiffness matrices, respectively, and $\{q\}_k$ and $\{Q_a\}_k$ are the generalized coordinates and aerodynamic force vectors at discrete time k, respectively.

Out-of-plane deflections along FOSSs can be computed from measured unsteady strain data $\{\epsilon\}_k$ using a piecewise least-squares method, an Akima spline, and a linear assumption, as described in the two-step approach [6]. These computed deflections along the fibers are combined with an FE model of the structure in order to interpolate and extrapolate the deflection and slope of the entire structure through the use of the System Equivalent Reduction and Expansion Process (SEREP) [13]. All of the degrees of freedom (DOF) in the FE model can be rearranged, as shown in Eq. (2):

$$\{q\}_k = \begin{Bmatrix} q_M \\ q_S \end{Bmatrix}_k = [\Phi]\{\eta\}_k = \begin{bmatrix} \Phi_M \\ \Phi_S \end{bmatrix}\{\eta\}_k \qquad (2)$$

where, $\{q_M\}_k$ is the master DOF at discrete time k. In this approach, deflections along the FOSS computed from the first step of the two-step approach [6] are defined as the master DOF. The remaining deflections and slopes over all of the structure are defined as slave DOFs at discrete time k, $\{q_S\}_k$. In Eq. (2), matrices $[\Phi_M]$ and $[\Phi_S]$ are eigen-matrices corresponding to master and slave DOFs, respectively, and $\{\eta\}_k$ is the orthonormalized coordinates vector at discrete time k. Therefore, Eqs. (3) and (4) are derived from Eq. (2).

$$\{q_M\}_k = [\Phi_M]\{\eta\}_k \qquad (3)$$

$$\{q_S\}_k = [\Phi_S]\{\eta\}_k \qquad (4)$$

In Eq. (3), changing the master DOF at discrete time k $\{q_M\}_k$ to the corresponding measured value $\{q_{Me}\}_k$, along the FOSS, gives Eq. (5):

$$\{q_{Me}\}_k = [\Phi_M]\{\eta\}_k \qquad (5)$$

where $\{q_{Me}\}_k$ is obtained from the first step of the two-step approach [6]. Pre-multiplying $[\Phi_M]^T$ to Eq. (5) with matrix inversion yields Eq. (6) for computing the orthonormalized coordinates vector at discrete time k:

$$\{\eta\}_k = ([\Phi_M]^T[\Phi_M])^{-1}[\Phi_M]^T\{q_{Me}\}_k, \qquad (6)$$

and the generalized coordinates vector $\{q\}_k$ of Eq. (7) is obtained from substituting Eq. (6) into Eq. (2).

$$\{q\}_k = \begin{bmatrix} \Phi_M \\ \Phi_S \end{bmatrix}([\Phi_M]^T[\Phi_M])^{-1}[\Phi_M]^T\{q_{Me}\}_k \qquad (7)$$

2.2 Computation of Velocity and Acceleration from Computed Wing Deflection

A simple harmonic motion assumption for the computation of wing acceleration works with undamped free vibration problems [7], but this assumption cannot handle the heavy damping issues associated with aeroelastic oscillation problems. Also, the orthonormalized coordinate vector $\{\eta\}_k$ used for the computation of velocities in Ref. [7] are not fully decoupled because of coupling between structural dynamics and unsteady aerodynamics.

A new approach for the computations of aeroelastic velocity and acceleration is proposed in this study. Velocity and acceleration vectors at each sensor location at discrete time k, $\{\dot{q}_{Me}\}_k$ and $\{\ddot{q}_{Me}\}_k$, of an aeroelastic structural motion are computed using Eq. (8) together with analytical derivatives with respect to time:

$$\{q_{Me}(t)\} = \{\tilde{q}_{Me}\} + \left\{ \sum_{i=1}^{nm} e^{-\sigma_i t} \left[A_{ij} cos(\omega_{di}t) + B_{ij} sin(\omega_{di}t) \right] \right\} \qquad (8)$$

where, $\sigma_i (= \zeta_i \omega_{ni})$ and ω_{di} are the i-th damping factor and damped frequency, respectively, and nm is the number of modes. A vector $\{\tilde{q}_{Me}\}$ represents the static equilibrium position of the unsteady wing motion. The coefficients A_{ij} and B_{ij}, $j = 1, 2, \ldots, n$, for the j-th row element of the vector can be fitted using a least-squares curve fitting technique [8, 9]. In this study, σ_i and ω_{di} are computed using an ARMA model, an on-line

parameter estimator, and a sine Butterworth low-pass filter [14]. It should be noted in Eq. (8) that σ_i and ω_{di} are estimated; therefore the least-squares curve fitting in this study is based on a linear fitting. From Eq. (8), velocity and acceleration are computed using analytical derivatives with respect to time t. The FE model is not used for the computation of $\{q_{Me}\}_k$, $\{\dot{q}_{Me}\}_k$, and $\{\ddot{q}_{Me}\}_k$.

Velocity and acceleration vectors over the entire structure are also computed using Eqs. (9) and (10) (SEREP transformation).

$$\{\dot{q}\}_k = \begin{bmatrix} \Phi_M \\ \Phi_S \end{bmatrix} ([\Phi_M]^T[\Phi_M])^{-1}[\Phi_M]^T\{\dot{q}_{Me}\}_k \quad (9)$$

$$\{\ddot{q}\}_k = \begin{bmatrix} \Phi_M \\ \Phi_S \end{bmatrix} ([\Phi_M]^T[\Phi_M])^{-1}[\Phi_M]^T\{\ddot{q}_{Me}\}_k \quad (10)$$

2.3 Computation of Aerodynamic Load from Wing Deflection, Velocity, and Acceleration

First, modal AIC matrices are computed at Mach number M and reduced frequencies κ_p ($\equiv \frac{\omega_p C}{2U}, p = 1, 2, \dots, m$) using lifting surface theory:

$$[A(\kappa_1)], [A(\kappa_2)], \dots, [A(\kappa_m)]$$

where C is the chord length at a typical section and U is a far-field airspeed. These modal AIC matrices can be approximated with respect to frequency, Laplace variable s, using an RFA. In this study, Roger's approximation, Eq. (11), is selected for the RFA.

$$[A(s)] = [D_0] + s[D_1] + s^2[D_2] + \sum_{j=1}^{LT} \frac{s[C_j]}{s+\Omega_j} \quad (11)$$

Substituting Eq. (2) into Eq. (1) and pre-multiplying $[\Phi]^T$ yields Eq. (12).

$$[\Phi]^T[M][\Phi]\{\ddot{\eta}\}_k + [\Phi]^T[G][\Phi]\{\dot{\eta}\}_k + [\Phi]^T[K][\Phi]\{\eta\}_k$$

$$= [\Phi]^T\{Q_a\}_k = \{N\}_k \quad (12)$$

The orthonormalized aerodynamic force vector $\{N(s)\}$ in Laplace-domain is in Eq. (13).

$$\{N(s)\} = q_D[A(s)]\{\eta(s)\} \quad (13)$$
$$= q_D \left([D_0]\{\eta(s)\} + s[D_1]\{\eta(s)\} + s^2[D_2]\{\eta(s)\} + \sum_{j=1}^{LT} \frac{s[C_j]\{\eta(s)\}}{s+\Omega_j} \right)$$

The time-marching algorithm for the computation of the orthonormalized aerodynamic force at discrete time k can be summarized as follows [12] in Eqs. (14) through (21):

$$\{N\}_k = q_D([D_0]\{\eta\}_k + [D_1]\{\dot{\eta}\}_k + [D_2]\{\ddot{\eta}\}_k + [C]\{x\}_k) \quad (14)$$

$$\{x\}_k = [E]\{x\}_{k-1} + [\theta][B]\frac{\{\dot{\eta}\}_k + \{\dot{\eta}\}_{k-1}}{2} \quad (15)$$

where, $[E] = e^{[A]T_a}$ \quad (16)

$$[\theta] = \int_0^{T_a} e^{[A](T_a - \tau)} d\tau \quad (17)$$

$$[A] = \begin{bmatrix} -\Omega_1 I & 0 & \dots & 0 \\ 0 & -\Omega_2 I & \dots & 0 \\ \vdots & \vdots & \ddots & \vdots \\ 0 & 0 & \dots & -\Omega_{LT} I \end{bmatrix} \quad (18)$$

$$[B] = \begin{bmatrix} I \\ I \\ \vdots \\ I \end{bmatrix} \quad (19)$$

$$[C] = [C_1 \ C_2 \ \dots C_{LT}] \quad (20)$$

$$\{x\}_k = \begin{Bmatrix} x_1 \\ x_2 \\ \vdots \\ x_{LT} \end{Bmatrix}_k \quad (21)$$

and T_a is a sampling time. Orthonormalized coordinate vectors $\{\eta\}_k$, $\{\dot{\eta}\}_k$, and $\{\ddot{\eta}\}_k$ are computed from Eqs. (22), (23), and (24).

$$\{\eta\}_k = ([\Phi_M]^T[\Phi_M])^{-1}[\Phi_M]^T\{q_{Me}\}_k \quad (22)$$

$$\{\dot{\eta}\}_k = ([\Phi_M]^T[\Phi_M])^{-1}[\Phi_M]^T\{\dot{q}_{Me}\}_k \quad (23)$$

$$\{\ddot{\eta}\}_k = ([\Phi_M]^T[\Phi_M])^{-1}[\Phi_M]^T\{\ddot{q}_{Me}\}_k \quad (24)$$

From Eq. (12), the generalized aerodynamic force vector at discrete time k, $\{Q_a\}_k$, is shown in Eq. (25).

$$\{Q_a\}_k = ([\Phi]^T)^{-1}\{N\}_k \qquad (25)$$

A rectangular matrix $[\Phi]^T$ can be inverted using a singular-value decomposition technique. The steps used to compute aerodynamic force from measured strain are depicted in Fig. 1.

In general, aerodynamic force vectors from a lifting surface theory are normal to the aerodynamic model configuration. Therefore, unsteady induced drag force as well as spanwise force can be defined using the surface normal vector during the unsteady wing surface oscillation, as shown in Fig. 2.

3 Results and Discussions

A cantilevered rectangular wing, shown in Fig. 3, was selected for the validation of the proposed approach. This wing, with 6% circular arc cross sections and an aspect ratio of 5.0 was built and tested at the NASA Langley Research Center (*Hampton, Virginia, USA*) in 1959 [15]. The model has a uniform chord length of 4.56 in, a span length of 11.5 in, and a thickness of 0.065 in aluminum insert covered with flexible plastic foam (Fig. 3). The material properties of the aluminum insert are assigned a Young's modulus, E, of 9.208 Msi; a shear modulus, G, of 3.837 Msi; and a mass density of 0.1 lb/in^3. The shaped lumped weights are used to match the local cross sectional weight distribution of the plastic foam. Therefore, the small lumped weights are used near the leading and trailing edges and the large lumped weights are used near the mid-chord area. Detailed material properties are shown in Table 1. To represent the six FOSSs, the model is fit with 300 beam elements (50 per each fiber) that compute axial strain along the length of the wing. These six simulated FOSSs are assumed to be zero weight with zero stiffness (Fig. 3).

The frequencies and mode shapes of this cantilevered wing model are computed using an MSC/NASTRAN code [11]. Measured and computed natural frequencies are summarized in Table 2. Unsteady aerodynamic forces as well as wing deflections and velocities are computed using the CFL3D code [10]. A computational fluid dynamics (CFD) grid configuration for the CFL3D computations based on the Euler grid is given in Fig. 4. The CFD grid is a multi-block

($97 \times 73 \times 57$) grid with H-H topology. The time step size of the unsteady CFL3D computation is 0.000060515 s, and a total of 10,240 time steps were used in this computation. The unsteady aerodynamic theory used in section 2.3 is based on a linear lifting surface theory, ZAERO code (*ZONA Technology Inc., Scottsdale, Arizona, USA*) [16]. Therefore, a subsonic Mach number should be selected for the CFL3D computer simulation to minimize a nonlinear transonic effect. Local Mach number distributions under steady-state conditions with CFL3D computer simulations are given in Fig. 5. In this figure, local Mach number distributions at Mach 0.714 are high subsonic conditions. Maximum local Mach number reaches the 0.8-0.9 range near the center chord, as shown in Fig 5(a). Supersonic sub-regions are observed in the Mach 0.875 case, that is, transonic speed, as shown in Fig. 5(b). Therefore, a Mach number of 0.714 with dynamic pressure of 1.455 psi was selected for the validation of the current approach. These CFD-based aerodynamic forces are assumed as the target forces in this study.

The MSC/NASTRAN code was used to calculate unsteady strains in this study, and these computed strains are considered as the measured strains. For the CFL3D computations, structural mode shapes should be provided at the CFD grid points. In this study, the structural grid points and the CFD grid points were connected using the interpolation elements, "RBE3 element" in MSC/NASTRAN terminology, instead of using a surface-splining technique. In the CFL3D code, unsteady aerodynamic force vectors are computed at the centroids of CFD cells. Therefore, a splining between structural grid points and these centroids is also needed for the transient response computations with the MSC/NASTRAN code. In this study, RBE3 elements are also created between structural grids and these centroids of CFD cells, as shown in Fig. 6. It should be noted that the well-known numerical problems associated with the Harder and Desmarais surface-spline technique [17] can be easily overcome through the use of the current technique with RBE3 elements.

The MSC/NASTRAN modal transient response analysis (solution 112) with 1,024 time steps and a step size of 0.00060515 s is used to

compute the strains, deflections, velocities, and accelerations. The structural deflection and velocity values at the leading edge of the wing-tip section obtained through the use of the CFL3D and MSC/NASTRAN codes are compared in Fig. 7. Excellent deflection and velocity matching are observed in this figure. Therefore, strain values computed from the MSC/NASTRAN code can be used as measured strain values to estimate the unsteady aerodynamic forces computed using the CFL3D computer simulation with the Euler equation.

Time histories of strain under different levels of white noise are shown in Fig. 8. Fig 8(a) shows time histories of strain at the leading edge of the wing-root section. Random white noise was added to the unsteady strain data to demonstrate the robustness of the proposed approach. The strain signal-to-noise ratio (SNR) is defined as shown in Eq. (26):

$$SNR \equiv 20 \times log_{10} \frac{\epsilon_{rms}}{n_{rms}} \qquad (26)$$

where, ϵ_{rms} and n_{rms} represent the root-mean-squared (RMS) level of the unsteady strain and added noise, respectively. In this study, the SNR of 10 dB, 6 dB, and 0 dB were used in the computer simulation. Corresponding time histories are shown in Figs 8(b), 8(c), and 8(d). The local SNR (LSNR) is defined as:

$$LSNR \equiv 20 \times log_{10} \frac{\epsilon_{max}}{n_{rms}} \qquad (27)$$

where, ϵ_{max} is the local maximum absolute unsteady strain value. In Fig. 8(d), the LSNR value is same with the SNR value near 0.33 s. The LSNR value is larger than SNR value before 0.33 s. The LSNR value becomes -9.8 dB near 0.59 s.

In this study, robustness of the proposed least-squares curve fitting method, Eq. (8), are tested using time histories of unsteady strain, shown in Fig. 8. A moving time window of 56 time steps was used in this curve fitting, as shown in Fig. 9. The least-squares curve fitting method in Eq. (8) is a nonlinear fitting problem; however, this nonlinear fitting problem becomes a linear problem when the damping factors and damped

aeroelastic frequencies, σ_i and ω_{di}, are provided. In this study, a sine Butterworth low-pass filter [14] with a cutoff frequency of 200 Hz is used to estimate reasonable frequencies and damping factors from unsteady strain data. The number of ARMA coefficients is seven and the sampling time for this on-line estimator is 0.004236 s (eight steps). In this study, a recursive least-squares method based on Bierman's U-D factorization algorithm with forgetting factor of 0.98 was used as an on-line parameter estimator [8]. Once fitted coefficients $\{\tilde{q}_{Me}\}$, A_{ij}, and B_{ij} are obtained based on the current 56 time steps, then deflections are predicted for the next eight time steps. These eight steps correspond to the one sampling period for the on-line parameter estimator. As shown in Fig. 9, the damping factors and damped aeroelastic frequencies, σ_i and ω_{di}, are updated with every sampling time step.

Time histories of Z deflection, velocity, and acceleration under 0 dB SNR are shown in Figs. 10, 11, and 12, respectively. The least-squares curve fitting starts after the converged damping factors and damped frequencies are obtained; thus, velocities and accelerations are not available until 400 steps (0.2414 s) as shown in Figs. 11 and 12. In Figs. 10, 11, and 12, the black solid lines, blue solid lines, and red dashed lines represent target values, corresponding deflection, velocity, and acceleration values before ($\{q_{Me}\}_k$, $\{\dot{q}_{Me}\}_k$, and $\{\ddot{q}_{Me}\}_k$) and after ($\{q\}_k$, $\{\dot{q}\}_k$, and $\{\ddot{q}\}_k$) using SEREP transformation, respectively.

The effect of the piecewise least-squares method for the computation of the unsteady deflection can be observed during the learning period as shown in Fig.10, as the solid blue line. Even with noisy strain data (LSNR of 8.7 dB to 1.6 dB), unsteady deflections are successfully obtained. The effect of the SEREP transformation can be also observed in Figs. 10, 11, and 12 as the blue solid line versus the red dashed line. Noise in the blue solid line becomes smoother after SEREP transformation is applied. Finally, the effect of the least-squares curve fitting method in Eq. (8) can be clearly observed before and after 0.2414 s, as shown in Fig. 10. Noise in unsteady deflection during the learning period is drastically reduced after the least-squares curve fitting is used. Wing deflection, velocity, and acceleration are in excellent agreement with corresponding target

values, as shown in Figs. 10, 11, and 12. The proposed least-squares curve fitting method together with the analytical time derivatives performed excellently even with an LSNR of -9.8 dB.

Modal AIC matrices are computed using the ZAERO code at Mach 0.714. The ZAERO-based unsteady aerodynamic model configuration is shown in Fig. 2(a). Reduced frequencies of 0.0, 0.006, 0.015, 0.035, 0.08, 0.13, and 0.26 were selected for this computation. Roger's approximation with four aerodynamic lag terms was used for an RFA of these modal AIC matrices. The element-by-element least-squares curve fitting with a constraint at the steady-state condition, reduced frequency of zero, was used in the Roger's approximation procedure. Aerodynamics lag frequencies were 11.81 Hz ($\kappa = 0.0177$), 47.22 Hz ($\kappa = 0.0707$), 106.2 Hz ($\kappa = 0.1591$), and 188.9 Hz ($\kappa = 0.2829$).

The total induced drag, spanwise, and lift forces obtained from the current approach under different levels of white noise are compared with the corresponding target aerodynamic forces from CFL3D computations in Figs 13, 14, and 15. The least-squares curve fitting method starts at 0.2414 s in Figs. 13, 14, and 15. It is interesting that the computed forces between time 0 to 0.2414 s are based on unsteady deflection only. Velocities and accelerations are assumed to be zero during learning period, as shown in Figs. 11 and 12. The effects of noise can be observed in Fig. 13. Computed total induced drag forces with an SNR of 0 dB is the most noisy result, as shown in Fig. 13(d).

The wing thickness effects on induced drag and spanwise forces, 0.0353 lbf and 0.0961 lbf respectively, were subtracted from the CFD-based target force to have zero force at steady-state condition in Figs 13 and 14. In general, the current approach based on lifting surface theory gives smaller forces than the target values in the cases of lift and spanwise forces. The computed induced drag forces are in excellent matching with the corresponding target drag force, as shown in Fig. 13.

6 Conclusions

In this study, unsteady aerodynamic forces were computed using simulated measured strain data. From unsteady strain information, unsteady structural deflections were computed using the two-step approach. Unsteady velocities and accelerations were computed using an AutoRegressive Moving Average model, on-line parameter estimator, low-pass filter, and a least-squares curve fitting method together with analytical derivatives with respect to time. The deflections, velocities, and accelerations at each sensor location are independent of structural and aerodynamic models. The distributed strain data together with the current proposed approaches therefore can be used as distributed deflection, velocity, and acceleration sensors.

The general structural deflections, velocities, and accelerations were converted to the orthonormalized coordinates to compute orthonormalized aerodynamic force vectors using modal aerodynamic influence coefficient (AIC) matrices. The modal AIC matrices were fitted in Laplace-domain using Roger's approximation. Laplace-domain aerodynamics were converted to the time-domain using a time-marching algorithm. The orthonormalized aerodynamic force vectors were transformed to the generalized coordinates using pseudo-matrix inversion based on singular-value decomposition. Finally, induced drag and spanwise forces were obtained using surface normal vectors. In general, computed aerodynamic forces based on the lifting surface theory in subsonic speeds are in good agreement with the target aerodynamic forces generated using CFL3D code with the Euler equation. This research demonstrates the feasibility of sensing induced drag and lift forces through the use of distributed sensor technology together with the fiber optic strain sensor. Thus, an active induced drag control system can be designed using these two computed aerodynamic forces, induced drag and lift, to improve the fuel efficiency of an aircraft.

In this study, interpolation elements ("RBE3 elements" in MSC/NASTRAN [*MSC Software Corporation, Newport Beach, California, USA*] terminology) between structural finite elements grids and the CFD grids and centroids were successfully incorporated with the unsteady aeroelastic computation scheme. The numerical

problems often associated with the Harder and Desmarais surface-splines technique thus are bypassed using the current technique with the RBE3 elements.

It should be emphasized that the deflection, velocity, and acceleration computation based on the proposed least-squares curve fitting method are validated with respect to the unsteady strain with LSNR of -9.8 dB. Therefore, the current methodology of computing unsteady aerodynamic forces can be applied to the actual flight-test data. The most critical technology for the success of the proposed approach is the robust on-line parameter estimator, since the least-squares curve fitting method depends heavily on aeroelastic system frequencies and damping factors.

References

[1] Washburn A. Drag Reduction Status and Plans - Laminar Flow and AFC. Presented at the AIAA Aerospace Sciences Meeting, Orlando, Florida, 2011.

[2] Ramakrishnan M., Rajan G., Semenova, Y. and Farrell G. Overview of Fiber Optic Sensor Technologies for Strain/Temperature Sensing Applications in Composite Materials. *Sensors*, Vol. 16, No. 99, 2016. DOI: 10.3390/s16010099.

[3] Igawa H. et al. Measurement of Distributed Strain and Load Identification Using 1500 mm Gauge Length FBG and Optical Frequency Domain Reflectometry. Proc. of SPIE, Vol. 7503, 2009. DOI: 10.1117/12.834236.

[4] Cusano A., Cutolo A., Nasser J., Giordano,M., Calabrò A. Dynamic Strain Measurements by Fibre Bragg Grating Sensor. *Sensors and Actuators A: Physical*, Vol. 110, Issues 1-3, pp. 276-281, 2004

[5] Liu T., Barrows D., Burner A. and Rhew R. Determining Aerodynamic Loads Based on Optical Deformation Measurements. AIAA-2001-0560, 2001.

[6] Pak, C.-g. Wing Shape Sensing from Measured Strain. *AIAA Journal*, Vol. 54, No. 3, pp. 1068-1077, 2016. DOI: 10.2514/1.J053986.

[7] Pak C.-g. and Truax R. Acceleration and Velocity Sensing from Measured Strain. AIAA 2016-1229, 2016. DOI: 10.2514/6.2016-1229.

[8] Pak C.-g. and Friedmann, P. New Time-Domain Technique for Flutter Boundary Identification. AIAA-92-2102, 1992. DOI: 10.2514/6.1992-2102.

[9] Bennett R. and Desmarais R. Curve Fitting of Aeroelastic Transient Response Data with Exponential Functions. NASA-SP-415, 1975.

[10] Krist S., Biedron R. and Rumsey C. CFL3D User's Manual (Version 5.0). NASA/TM-1998-208444, 1998.

[11] *MSC/NASTRAN Quick Reference Guide Version 69*, MacNeal-Schwendler Corporation, Los Angeles, California, 1996.

[12] Pak C.-g., Friedmann P. and Livne E. Digital Adaptive Flutter Suppression and Simulation Using Approximate Transonic Aerodynamics. *Journal of Vibration and Control*, Vol. 1, No. 4, pp. 363-388, 1995.

[13] O'Callahan J., Avitabile P. and Riemer, R. System Equivalent Reduction Expansion Process. 7th International Modal Analysis Conference, Las Vegas, pp. 29-37, 1989.

[14] Otnes R. *Applied Time Series Analysis: Volume 1: Basic Techniques* John Wiley & Sons Inc., New York, pp. 421-422, 1978.

[15] Doggett R. Jr., Rainey A. and Morgan H. An Experimental Investigation of Aerodynamic Effects of Airfoil Thickness on Transonic Flutter Characteristics. NASA-TMX-79, 1959.

[16] ZAERO User's Manual Version 8.2, ZONA Technology, Inc., Scottsdale, Arizona, 2008.

[17] Harder R. and Desmarais R. Interpolation Using Surface Spines. *AIAA Journal of Aircraft*, Vol. 9, No. 2, pp. 189-191, 1972. DOI: 10.2514/3.44330.

7 Contact Author Email Address

mailto:Chan-gi.Pak-1@nasa.gov

Copyright Statement

Tables

Properties of aluminum insert	Number
Young's modulus, E	9207766 psi
Shear modulus, G	3836570 psi
Density	0.1 lb/in^3
Total weight	0.3806 lb
Xcg	2.28 inch
Ycg	5.75 inch
Thickness	0.065 inch

Table 1. Detailed material properties of the cantilevered plate wing

Mode	Measured (Hz)	Computed (Hz)	Comment
1	14.29	14.29	First bending
2	80.41	80.17	First torsion
3	89.80	89.04	Second bending

Table 2. Measured and computed natural frequencies

Figures
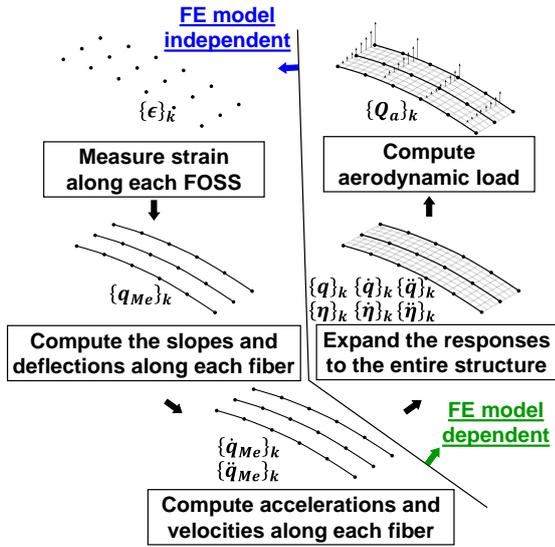
Fig. 1. Steps used to compute aerodynamic force from measured strain.
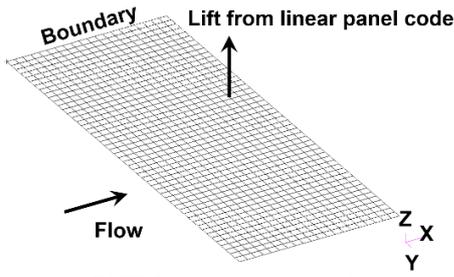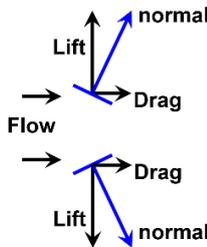
Fig. 2. Definition of the unsteady aerodynamic forces from a linear lifting surface theory.
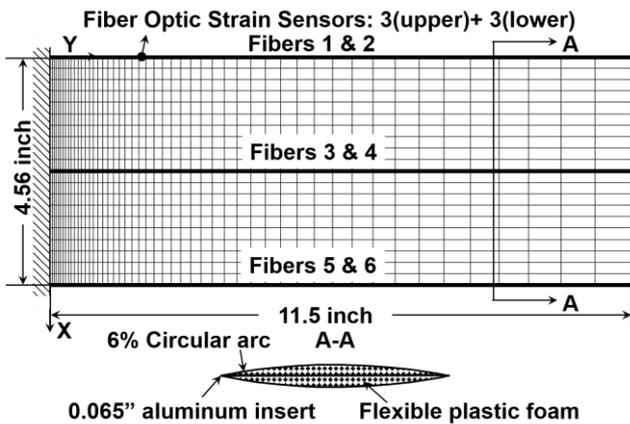
Fig. 3. Cantilevered rectangular wing with six FOSSs.
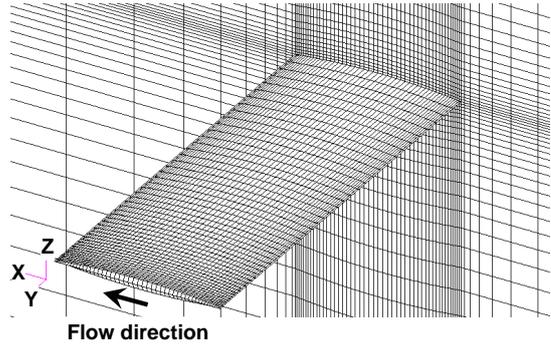
Fig. 4. A CFD grid for CFL3D computations based on Euler grid.
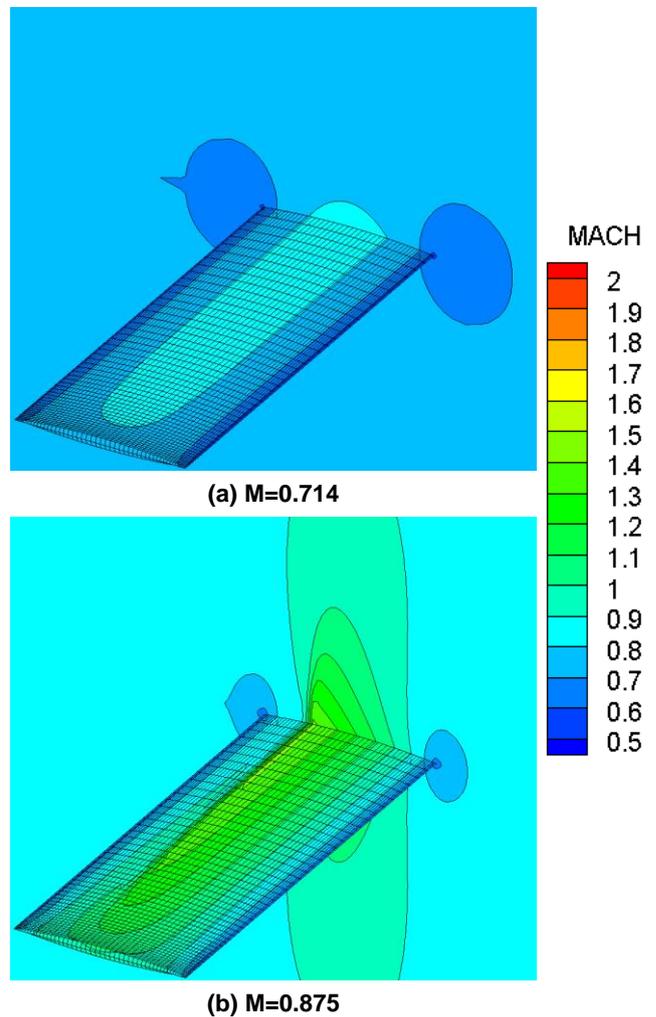
Fig. 5. Local Mach number distributions at Mach 0.714 and 0.875.
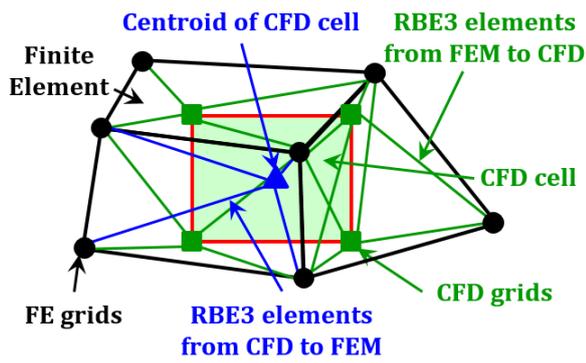
Fig. 6. RBE3 elements between structural grid points and CFD grids and centroids.
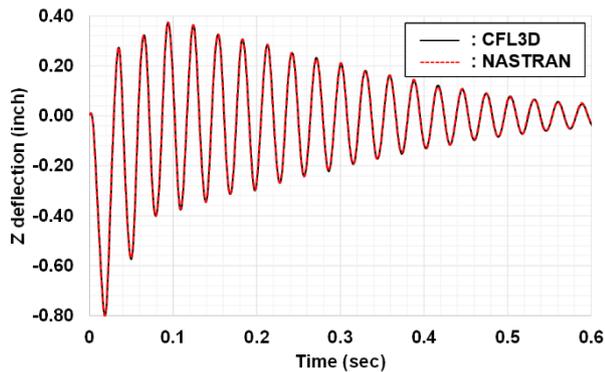
(a) Deflection
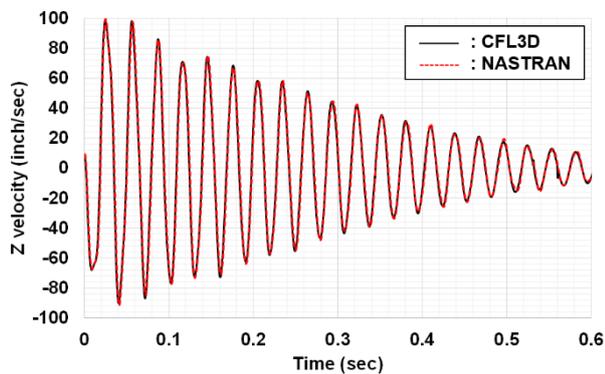
(b) Velocity

Fig. 7. Deflection and velocity comparisons using CFL3D and MSC/NASTRAN codes.
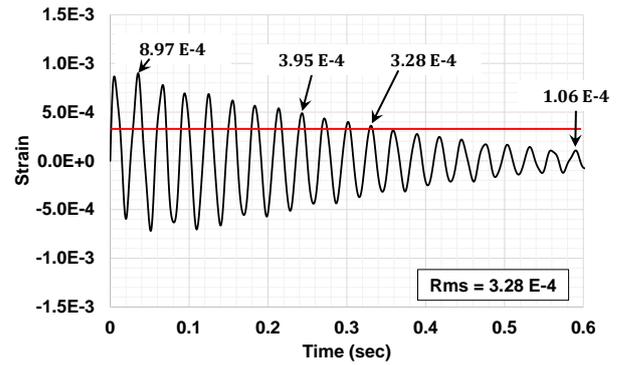
(a) Without noise
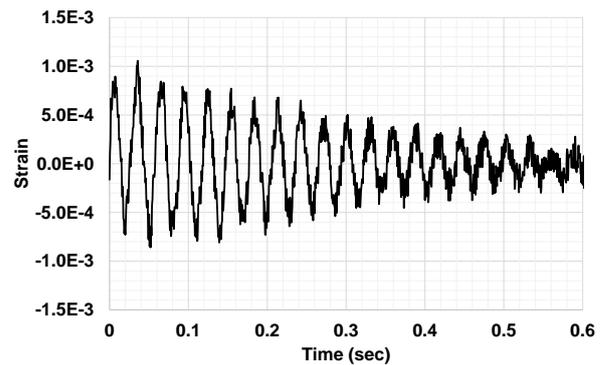
(b) SNR = 10 dB
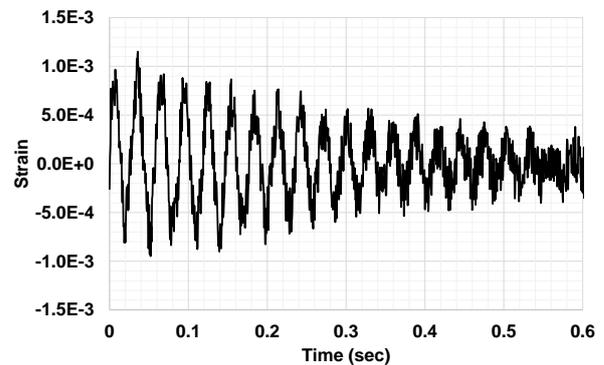
(c) SNR = 6 dB
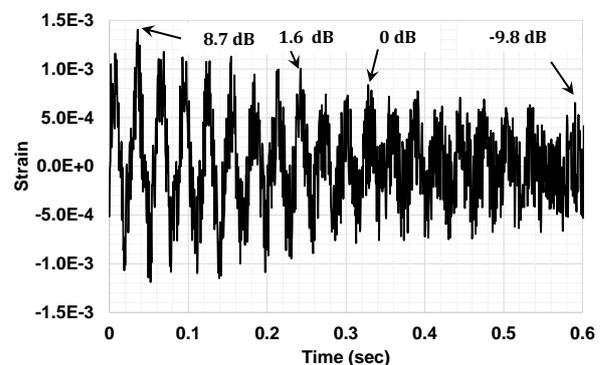
(d) SNR = 0 dB

Fig. 8. Time histories of strain under different levels of random white noise.
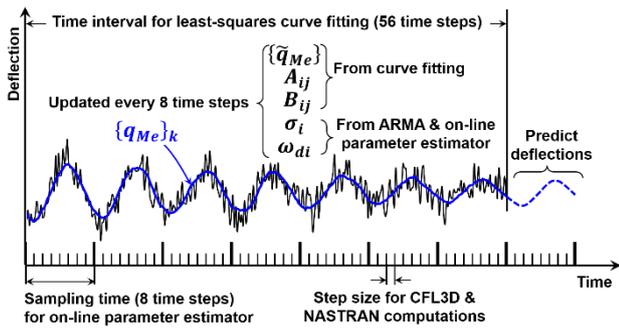
Fig. 9. Summary of the least-squares curve fitting and deflection prediction.
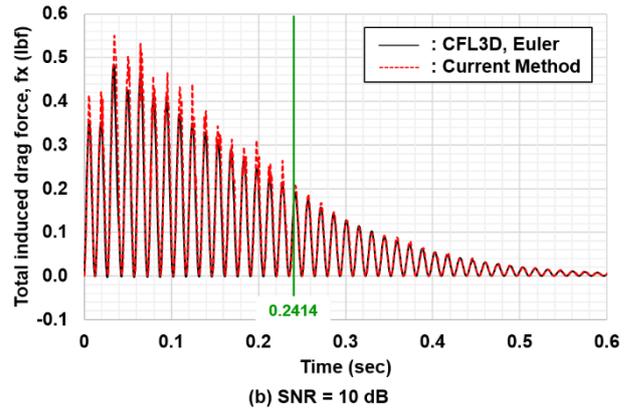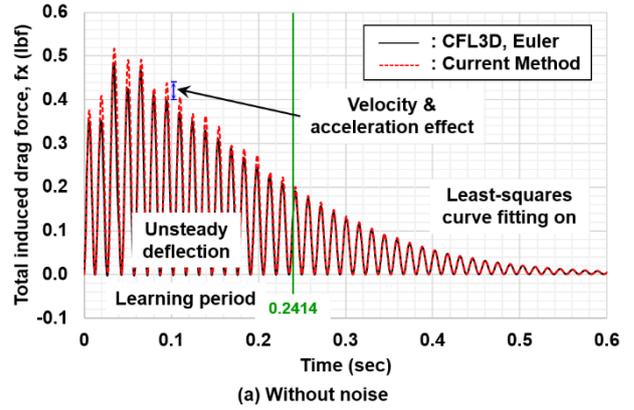
Fig. 10. Time histories of Z deflection under SNR = 0 dB.
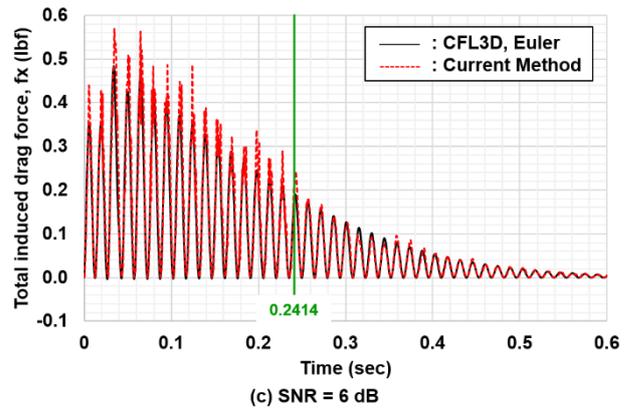
Fig. 11. Time histories of Z velocity under SNR = 0 dB.

Fig. 12. Time histories of Z acceleration under SNR = 0 dB.

(a) Without noise

(b) SNR = 10 dB

(c) SNR = 6 dB

(d) SNR = 0 dB

Fig. 13. Time histories of total induced drag force under different levels of random white noise.
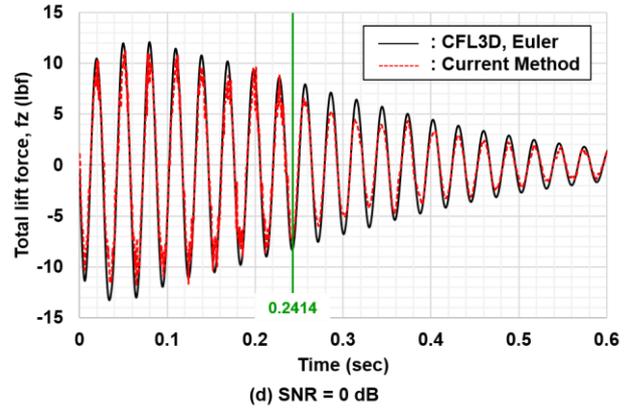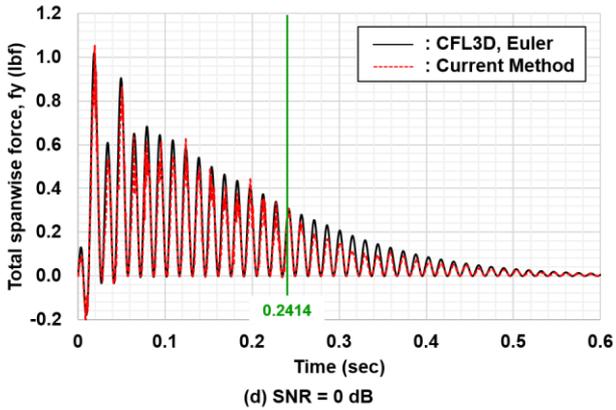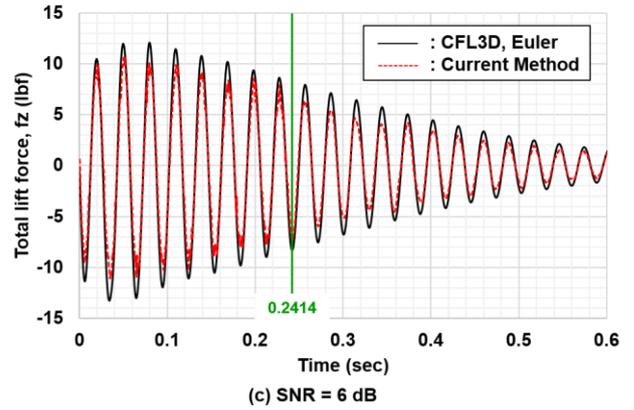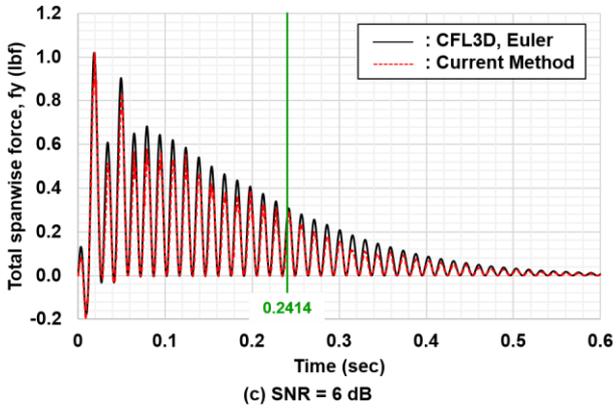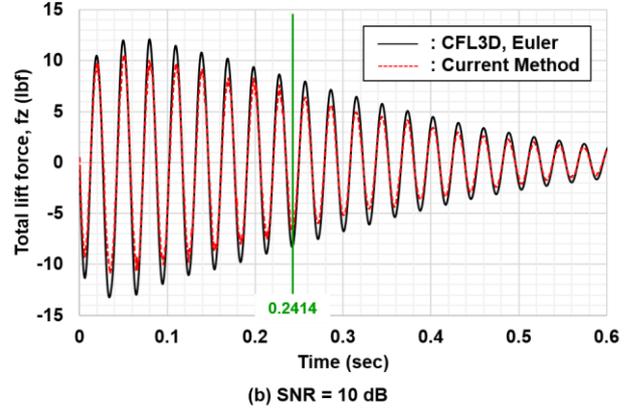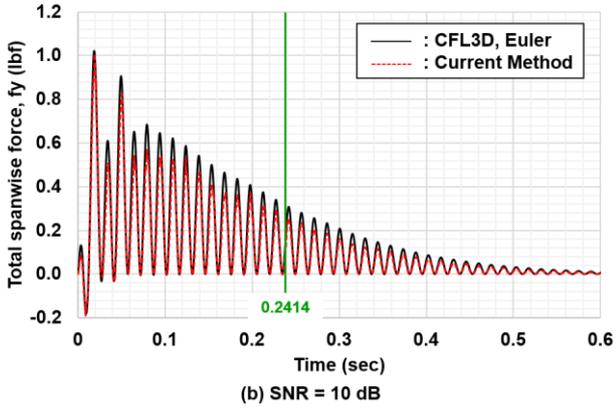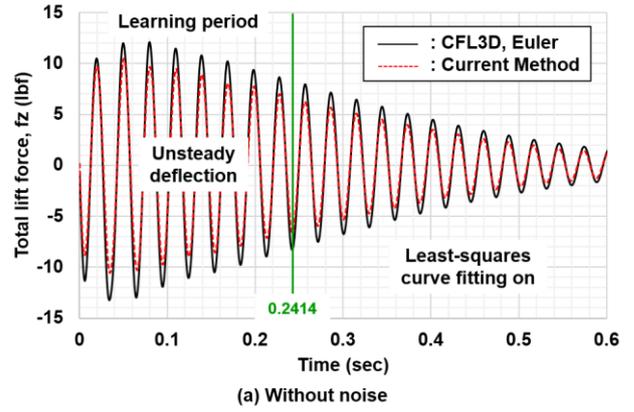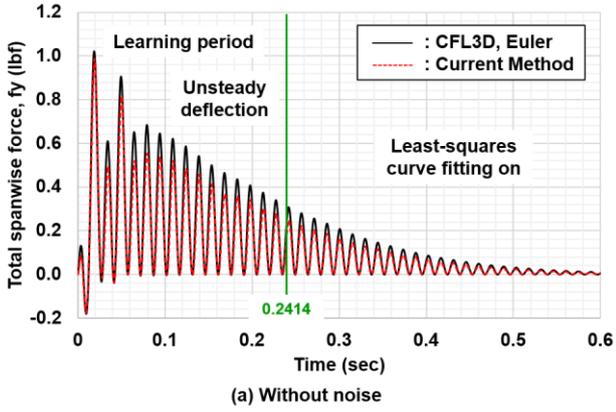
Fig. 14. Time histories of total spanwise force under different levels of random white noise.

Fig. 15. Time histories of total lift force under different levels of random white noise.